ADVANCES IN NUCLEAR SCIENCE AND APPLICATIONS

Volume 1, No. 2 (2025), P. 120-130

Thermal behavior of TiCN carbonitride doped with Zr, Nb and Si

S. Isayeva[1,2], R. Turar[3,4],
A. Nygymanova[3], D. Mirzayeva[4], T. Mauyey[3,*]
[1]Institute for Space Research of Natural Resources Azerbaijan
National Aerospace Agency, Baku, Azerbaijan
[2]Azerbaijan Technical University, Baku, Azerbaijan
[3]L.N. Gumilyov Eurasian National University, Astana, Kazakhstan
[4]Joint Institute for Nuclear Research, Dubna, Russia
e-mail: tileubek_1220@mail.ru

DOI: 10.63907/ansa.v1i2.33
Received 1 June 2025

Abstract

In this study, the oxidation kinetics, diffusion rates, and oxide layer thicknesses of TiZrCN, TiSiCN, and TiNbCN compounds synthesized on a high-purity biphasic Ti_6Al_4V alloy substrate were investigated over the temperature range from room temperature to 1250 K. The temperature-dependent growth of oxide layers on the active surface and the corresponding activation energies were determined based on Arrhenius plots. Differential scanning calorimetry (DSC) analysis was employed to examine the mechanisms governing changes in thermodynamic functions and heat capacity across the investigated temperature range.

Keywords: Carbonitride structures, nanomaterials, oxidation kinetics, activation energy, DSC.

1 Introduction

In recent years, insulators based on ceramic and nitride compounds have gained significant attention, particularly in nuclear technology applications, due to their superior insulating performance, thermal stability, and radiation resistance compared to conventional materials [1, 2, 3, 4, 5]. Ceramic materials are extensively employed as key structural components in plasma-facing devices [6, 7, 8]. A critical consideration in these environments is the exposure of materials to various forms of ionizing radiation generated within the systems [9, 10, 11]. Therefore, materials intended for use under radiation must exhibit enhanced mechanical, thermal, and structural stability [12, 13, 14].

This study focuses on the behavior of ceramics under irradiation and elevated temperatures. Both temperature and plasma conditions influence the ion slowing-down length in solids, emphasizing the importance of understanding ion"material interactions in plasma environments [15, 16, 17, 18]. The present investigation examines ion energy, plasma temperature, and the flux of fast ions produced during plasma heating in Tokamak systems [19]. Based on these considerations, experimental evaluation of temperature effects on various ceramic materials becomes essential [20].

Among different coating systems synthesized by physical vapor deposition (PVD) techniques, carbonitrides have shown outstanding mechanical, tribological, and oxidation resistance, making them highly suitable for advanced applications [21, 22, 23, 24, 25, 26]. The structure of carbonitride coatings comprises carbon (C) and nitrogen (N), both of which contribute to optimizing the material's functional properties [27, 28, 29, 30, 31, 32]. In particular, TiCN coatings demonstrate enhanced mechanical strength and thermal stability compared to their binary counterparts, TiC and TiN [33]. TiC is known for its high melting point, strong interfacial adhesion, and low internal stress levels [34, 35, 36].

Carbonitride coatings can be engineered in a variety of architectures"including single-layer, multilayer, and compositionally graded configurations"allowing precise control over structural and chemical properties [37, 38, 39, 40].

Among carbonitrides such as TiCN, ZrCN, NbCN, and CrCN, ternary coatings containing a transition metal are the most widely used for industrial applications [42, 43, 19]. Ti(Metal)CN as a commercial product requires comprehensive investigation. By introducing various metallic and non-metallic elements into the ternary matrix, it becomes possible to develop next-generation carbonitrides. The incorporation of minor amounts of Zr, Nb, and Si into the TiCN matrix has been shown to reduce internal stresses while enhancing adhesive characteristics. Furthermore, this modification significantly improves the material's corrosion resistance properties in chemically corrosive environments [44].

The alloying effects observed in PVD-synthesized carbonitride coatings such as TiCrCN [45], TiSiCN [46, 47, 48, 49], TiCrNbCN [50], and TiAlSiCN [51, 52, 53] enhance their functional properties for diverse applications [54, 55, 56]. Given the pivotal role of carbonitrides in advancing science and technology, their production technologies can be tailored to meet specific requirements across fields [57, 58, 59, 60].

Research on TiN, ZrC, ZrN, ZrCN, and TiC compounds demonstrates that these materials exhibit oxidation resistance across a wide temperature range and superior mechanical properties under various conditions [61]. However, in recent studies, cathodic arc deposition has been employed to create TiZrCN, TiZrSiCN, and TiZrNbCN surfaces, though their temperature-dependent oxidation mechanisms remain unexplored.

The primary objective of this study is to investigate the oxidation mechanisms of carbonitride coatings (TiZrCN, TiSiCN, and TiNbCN) synthesized via cathodic arc evaporation, where nanostructured Zr, Nb, and Si are incorporated into the TiCN matrix.

2 Experimental part

In the experiments, the value of the heat flow is treated as a function of temperature, characterizing the thermal transitions, chemical reactions, and heat capacity that occur due to the amount of heat transferred to the sample [62]. It is possible to determine the dependency of heat capacity on temperature and the mechanism of change of thermodynamic functions based on the specified value of heat flow [63, 64]. Despite the various approaches in DSC studies, the key physical parameter for an accurate transition from heat flow to heat capacity is the determination of the heat capacity of the reference material [65]. Based on known values of heat capacity, it is possible to establish the temperature dependencies of thermodynamic functions [66].

The cathodic arc deposition method was used to create thin film layers on the surface of the materials studied. Ti85%-Nb15%, Ti85%-Zr15% (99.99% pure), and Ti88%-Si12% cathodes were employed. The deposition conditions were selected with:

- (C+N)/(metal+Nb, Zr, Si) ratio of 0.6–0.8,
- C/N ratio of 0.4 (lower stoichiometric) and 1.6 (upper stoichiometric),
- Concentration range of 4–12% for Zr, Nb, and Si.

The experiments were conducted on TiZrCN, TiSiCN, and TiNbCN compounds. The average density of the synthesized materials was measured to be 6.78 g/cm^3, with specimen dimensions of $4 \times 4 \times 3$ mm (National Institute of Research and Development for Optoelectronics). The nanostructures of Zr, Nb, and Si incorporated into the TiCN matrix exhibited particle sizes ranging from 5 to 20 nm.

Differential scanning calorimetry (DSC) measurements were carried out using a STA 6000 simultaneous thermal analyzer (Perkin Elmer). Standard adiabatic calorimetric measurements were performed under an argon atmosphere with a controlled flow rate of 20ml/min. The heating rate was maintained at $5°\text{C/min}$ across the temperature interval of 300 to 700K. Cooling was facilitated using the integrated cooling system of the PolyScience analyzer, coupled with a digital temperature controller.

3 Results and Discussion

The high-temperature oxidation mechanism of carbonitride-based materials is strongly influenced by parameters such as specific surface area, purity level, and particle size [67]. Moreover, the introduction of nanostructured dopants, including Zr, Nb, and Si, adds further complexity to the interpretation of oxidation kinetics and phase evolution [68]. Generally, the oxidation behavior of TiCN-based compounds can be interpreted as a synergistic process, combining the intrinsic oxidation of the

TiCN matrix with additional oxidation mechanisms induced by the incorporated nanostructures.

The overall oxidation degree can be expressed as:

$$\alpha_{\text{total}} = \alpha_{\text{Zr,Nb,Si}} + \alpha_{\text{TiCN}},$$

where α_{total} is the total oxidation degree, $\alpha_{\text{Zr,Nb,Si}}$ is the contribution from oxidation of the Zr, Nb, and Si additives, and α_{TiCN} is the oxidation degree of the base TiCN matrix.

The total oxidation degree α_s is calculated using the expression:

$$\alpha_s = \frac{\Delta W}{\Delta W_{\text{th}}(\infty)},$$

where ΔW is the temperature- and time-dependent mass change, and $\Delta W_{\text{th}}(\infty)$ is the theoretical mass gain associated with complete oxidation to ZrO_2, Nb_2O_5, SiO_2, and TiO_2 in the TiZrCN, TiSiCN, and TiNbCN systems.

All experiments were conducted using thin-film specimens with dimensions of $5 \times 5 \times 4$ mm. Fig. 1 presents the temperature dependence of oxidation rates for TiCN, TiZrCN, TiSiCN, and TiNbCN compounds.

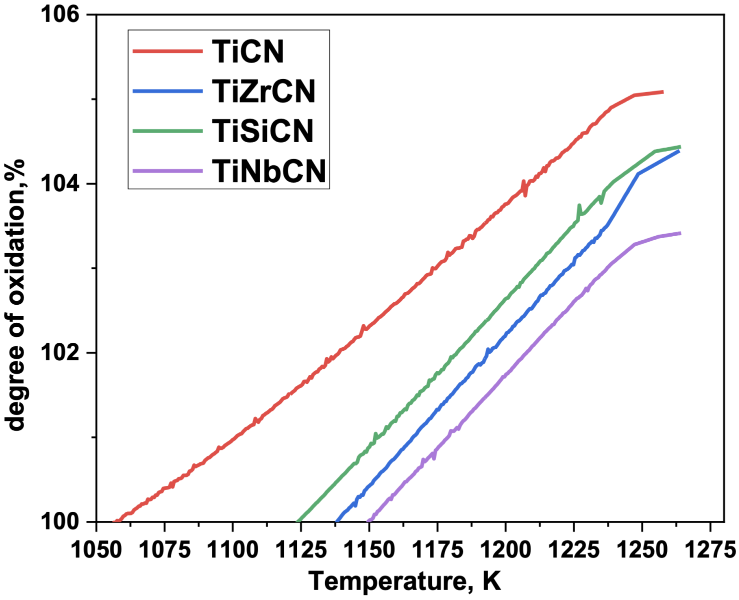

Figure 1: Temperature dependence of oxidation rates for TiCN, TiZrCN, TiSiCN, and TiNbCN coatings.

As shown in Fig. 1, the onset of oxidation for the TiCN compound occurs at 1048K, whereas for the TiZrCN, TiSiCN, and TiNbCN samples, oxidation initiates at elevated temperatures of $T \geq 1125$ K. The observed differences in mass change profiles among the samples can be partially attributed to the thermal decomposition of water vapor adsorbed from the ambient environment onto the specimen surfaces.

The oxidation process can be divided into two distinct regimes: (1) an initial rapid oxidation stage and (2) a subsequent quasi-stable regime. The transition between these regimes is notably influenced by the incorporation of Zr, Nb, and Si nanostructures into the TiCN matrix. The rapid oxidation phase occurs within the temperature range $1050 \leq T \leq 1250$ K, while the stable plateau region becomes prominent above $T \geq 1125\,K$. The critical oxidation temperature is identified as 1250K. The relatively low oxidation rates observed in the latter regime suggest a predominantly passive oxidation mechanism.

In the initial oxidation regime, the formation of protective oxide layers, including Zr_2O_3, Nb_2O_5, SiO_2, and TiO_2, occurs more actively. While the TiCN sample reaches an oxidation level of 5.5%, this value is reduced to 4.3% for the TiZrCN, TiSiCN, and TiNbCN samples, indicating an enhanced oxidation resistance attributable to the nanostructured dopants. This behavior supports the hypothesis of a dual-stage oxidation mechanism.

Beyond the critical temperature, active-phase oxidation is largely complete [69]. The kinetics of oxidation and the determination of activation energy require time-resolved analysis, as the oxidation rate is affected by multiple interdependent variables. In the early stages, oxidation progresses rapidly, while at elevated temperatures, the cumulative effects become more pronounced due to the presence of nanomaterials. Above 1250 K, the oxidation rates for all samples converge, suggesting saturation in the oxidation process.

The temperature range of $1050 \leq T \leq 1250$ K represents a thermally stable regime in which no significant dynamic changes in heat flow are observed. The TiCN sample demonstrates primarily non-isothermal oxidation behavior, yet linear oxidation is observed across the entire temperature range until reaching a critical limit.

The oxidation process is surface-dominated, as evidenced by the dependence of oxidation depth on surface characteristics. Key parameters influencing this include temperature, molar mass of both the base material and its oxidation products, specific surface area, and particle size. Considering the formation of Zr_2O_3, Nb_2O_5, SiO_2, and TiO_2 as primary oxidation products, the depth of the resulting oxide layer and the corresponding oxidation penetration can be quantified using the following expression:

$$Depthofoxidation(nm) = \left(\frac{\triangle W\%}{100\,S}\right) \times \left(\frac{M_{sample}}{2[M_{oxid}] - M_{sample}}\right) \times \frac{1}{d}, \tag{1}$$

where $\triangle W$ is weight of sample, S is the surface area of sample, M_{sample} is the molecular weight of sample, M_{oxid} is the molecular weight of oxides, and d is the density of samples. The temperature-dependent evolution of oxide layer thickness (1050-1250 K) in TiCN, TiZrCN, TiSiCN, and TiNbCN systems is shown in Fig. 2.

As anticipated, the oxidation depth follows a dual-mechanism behavior in the 1050-1250 K temperature range after incorporation of Zr, Nb, and Si nanoparticles. In the TiCN sample, both the oxidation rate and the resulting surface oxide layer approach stabilization in the high-temperature regime. This dependence reveals that the TiCN sample develops an oxide layer thickness of approximately 20 nm. However, in materials modified with Zr, Nb, and Si nanoparticles, the 'critical threshold value of oxide layer thickness' manifests at varying depths and magnitudes, demonstrating composition-dependent oxidation resistance. Additionally, the specific surface area is a critically important factor affecting the oxidation rate, and the high degree of chemical purity of the material significantly influences oxidation behavior. The observed linearity and stable regime in the oxidation process are explained by the mechanism of the chemical reaction occurring on the surface. In many cases, the

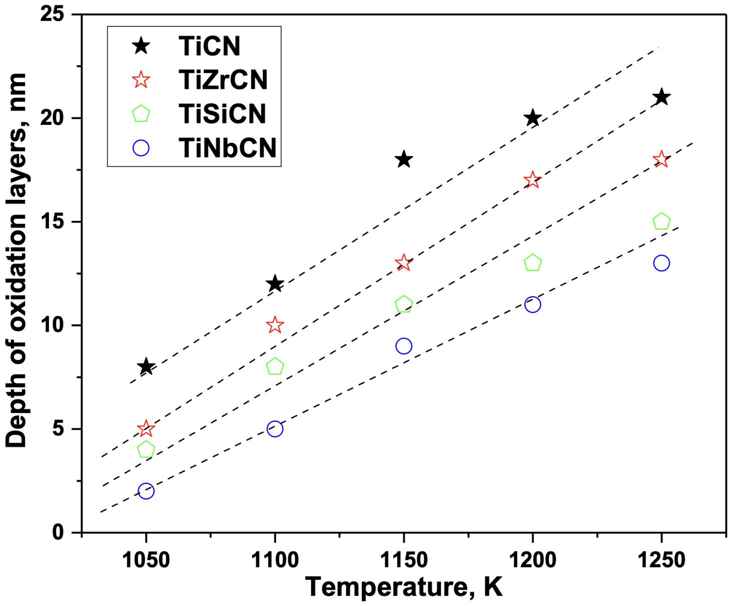

Figure 2: Oxide layer growth kinetics of TiCN-based systems (TiZrCN, TiSiCN, TiNbCN) as a function of temperature (1050-1250 K).

mechanism of oxide layer formation on the surface follows various kinetic laws. In physicochemical processes, activation energy values are used to explain oxidation kinetics. At elevated temperatures, the oxidation diffusion rate is observed to increase significantly. Furthermore, the high melting points of Zr_2O_3, Nb_2O_5, SiO_2 , and TiO_2 oxides contribute to enhanced diffusion rates during oxidation. More specifically, this leads to cumulative oxidation reactions. Fig. 3 presents Arrhenius plots for the oxide layers formed on the surface of TiCN, TiZrCN, TiSiCN, and TiNbCN compounds. The logarithmic values of the diffusion rate constants (lnk) are plotted against the inverse temperature (1000/T) to characterize the temperature dependence.

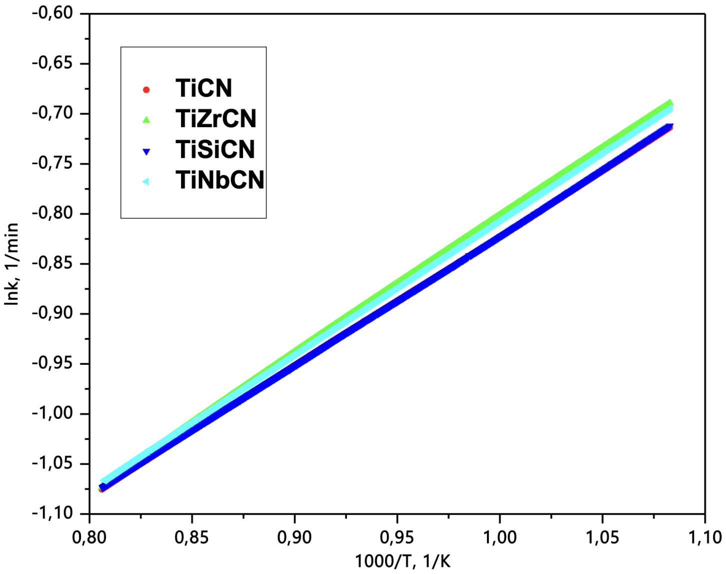

Figure 3: Arrhenius cruves of TiCN-based systems (TiZrCN, TiSiCN, TiNbCN) at (1050-1250 K) temperature range.

The activation energy for oxidation was found to be 12.5 kJ/mol for the TiCN sample, and $10.2\ \mathrm{kJ/mol}$, $9.58\ \mathrm{kJ/mol}$, and $8.74\ \mathrm{kJ/mol}$ for the TiZrCN, TiSiCN, and TiNbCN compounds, respectively. These decreasing activation energy values suggest that, upon doping with Zr, Nb, and Si nanoparticles, the materials exhibit enhanced reactivity at elevated temperatures, accompanied by a gradual reduction in their structural purity. The incorporation of nanostructured elements introduces active centers that alter the thermal behavior of the compounds. These centers facilitate accelerated energy-level transitions with increasing temperature, thereby influencing thermophysical characteristics.

To further investigate these effects, differential scanning calorimetry (DSC) analyses were carried out under ambient atmospheric conditions in an argon environment at a heating rate of $2^{\circ}\mathrm{C/min}$. The DSC profiles reveal that heat flux is mediated via multiple mechanisms. Transformation kinetics observed in the DSC spectra exhibit two characteristic regimes. Above $T \geq 1050$ K, the formation of oxide layers on the material surface generates prominent exothermic peaks.

Experimental results confirm that nitride-based materials are inherently reactive with atmospheric oxygen and water vapor [70]. The ratio of decomposition to oxidation reactions varies significantly depending on environmental factors. Moreover, disruptions in the crystalline structure notably impact thermal conductivity through phonon“phonon scattering mechanisms [71], which may explain the more linear and reduced heat transfer signals observed in the DSC spectra of TiZrCN, TiSiCN, and TiNbCN.

To calculate thermodynamic fields, known temperature-dependent heat capacity functions were employed [16]. The evolution of thermodynamic functions for each compound was derived based on established calorimetric relationships [22]. In nitride-based materials, these functions exhibit significant magnitudes during chemical transformation processes and are strongly temperature-dependent [72]. Each thermodynamic quantity associated with oxidation reactions consists of both linear and nonlinear components. Entropy, while not a directly measurable physical parameter, serves as an important descriptor of thermal mobility within the material. As temperature increases, entropy for the compounds reaches values on the order of $1.7\ \mathrm{J/(mol \cdot K)}$.

4 Conclusions

Research on TiCN, TiZrCN, TiNbCN, and TiSiCN compounds demonstrates that these materials exhibit high oxidation resistance over a broad temperature range. For pure TiCN coatings, the onset of oxidation is observed at approximately 1048 K. In contrast, for TiZrCN, TiSiCN, and TiNbCN coatings, oxidation initiates at higher temperatures, exceeding 1125 K. This shift suggests that the incorporation of Zr, Nb, and Si nanostructures into the TiCN matrix significantly enhances the thermal stability of the material.

The oxidation process generally follows a two-stage mechanism: an initial rapid oxidation phase, followed by a more stable passive oxidation regime. The rapid oxidation occurs within the temperature range of 1050 K $\leq$ T $\leq$ 1250 K, while the transition to a stable oxidation region begins at T $\geq$ 1125 K. The critical oxidation temperature for all compounds is identified at approximately 1250 K.

Within the stable region, the low observed oxidation percentages indicate a predominantly passive oxidation mechanism. However, in the initial temperature interval, the active formation of surface oxide layers, including ZrO_2, Nb_2O_5, SiO_2, and TiO_2, is more pronounced. At 1250 K, the total oxidation level reaches approximately 5.5% for TiCN, whereas it remains lower (around 4.3%) for TiZrCN, TiSiCN, and TiNbCN coatings.

Furthermore, the oxidation rate and the growth of the surface oxide layer in the TiCN sample tend to stabilize at elevated temperatures, suggesting the formation of a dense, protective oxide scale. The thickness of this oxide layer in TiCN is estimated to be on the order of 20 nm. In contrast, for TiZrCN, TiNbCN, and TiSiCN coatings, the presence of dopant nanoparticles alters the kinetics and morphology of oxide formation, with the so-called "critical threshold thickness" of the oxide layer varying across different materials and depths.

Acknowledgements

This research has been funded by the Science Committee of the Ministry of Science and Higher Education of the Republic of Kazakhstan (Grant No. AP27511571).

References

[1] S. K. Sharma, K. K. Saxena, K. H. Salem *et al.*, Adv. Mater. Process. Technol. **10**, 277 (2022).

[2] J. Qin, X. Chen, Y. Wang *et al.*, Metals **12**, 1420 (2022).

[3] L. Chen, Y. X. Xu, L. J. Zhang, Surf. Coat. Technol. **285**, 146 (2016).

[4] R. W. Harrison, W. E. Lee, Adv. Appl. Ceram. **115**, 294 (2016).

[5] J. Adachi, K. Kurosaki, M. Uno *et al.*, J. Alloys Compd. **399**, 242 (2005).

[6] H. Mao, F. Shen, Y. Zhang *et al.*, Coatings **11**, 1444 (2021).

[7] M. N. Mirzayev, Mod. Phys. Lett. B **34**, 2050395 (2020).

[8] M. N. Mirzayev, E. Demir, K. F. Mammadov *et al.*, J. Phys. **94**, 110 (2020).

[9] M. N. Mirzayev, E. Popov, E. Demir *et al.*, J. Alloys Compd. **834**, 155119 (2020).

[10] F. G. Agayev, S. H. Jabarov, G. Sh. Ayyubova *et al.*, J. Supercond. Nov. Magn. **33**, 2867 (2020).

[11] S. R. Azimova, N. M. Abdullayev, Y. I. Aliyev *et al.*, J. Korean Phys. Soc. **77**, 240 (2020).

[12] M. N. Mirzayev, Int. J. Mod. Phys. B **34**, 2050160 (2020).

[13] E. Demir, M. N. Mirzayev, A. B. Tugrul *et al.*, Surf. Rev. Lett. **27**, 1950169 (2020).

[14] S. R. Azimova, N. M. Abdullayev, Y. I. Aliyev *et al.*, Mod. Phys. Lett. B **34**, 2050156 (2020).

[15] E. P. Popov, A. N. Chernikov, A. I. Beskrovnyi *et al.*, J. Phys. Conf. Ser. **1492**, 012054 (2020).

[16] M. N. Mirzayev, Vacuum **173**, 109162 (2020).

[17] F. G. Agayev, S. H. Jabarov, G. Sh. Ayyubova *et al.*, Physica B **580**, 411772 (2020).

[18] M. N. Mirzayev, Ceram. Int. **46**, 2816 (2020).

[19] S. H. Jabarov, Y. I. Aliyev, T. M. Ilyasli *et al.*, Integr. Ferroelectr. **221**, 180 (2021).

[20] M. N. Mirzayev, B. A. Abdurakhimov, E. Demir *et al.*, Physica B **611**, 412842 (2021).

[21] M. N. Mirzayev, Radiat. Phys. Chem. **180**, 109244 (2021).

[22] E. Demir, M. N. Mirzayev, E. P. Popov *et al.*, Vacuum **184**, 109934 (2021).

[23] F. G. Agayev, S. V. Trukhanov, An. V. Trukhanov *et al.*, J. Therm. Anal. Calorim. **147**, 14107 (2022).

[24] T. T. Thabethe, S. A. Adeojo, M. N. Mirzayev *et al.*, Nucl. Instrum. Methods Phys. Res. B **527**, 58 (2022).

[25] D. R. Belichko, T. E. Konstantinova, G. K. Volkova *et al.*, Mater. Chem. Phys. **287**, 126237 (2022).

[26] E. Demir, E. Popov, M. Mirzayev *et al.*, Int. J. Refract. Met. Hard Mater. **106**, 105865 (2022).

[27] M. N. Mirzayev, A. A. Donkov, E. A. Popov *et al.*, Nanomaterials **12**, 2644 (2022).

[28] D. Neov, L. Slavov, A. A. Donkov *et al.*, Nucl. Mater. Energy **31**, 101201 (2022).

[29] A. S. Doroshkevich, A. I. Lyubchyk, B. L. Oksengendler *et al.*, Nanomaterials **12**, 1783 (2022).

[30] M. N. Mirzayev, L. Slavov, A. Donkov *et al.*, Radiat. Phys. Chem. **194**, 109988 (2022).

[31] P. Horodek, K. Siemek, M. N. Mirzayev *et al.*, Acta Phys. Pol. A **142**, 702 (2022).

[32] F. G. Agayev, A. V. Trukhanov, S. V. Trukhanov *et al.*, Phys. Status Solidi B **259**, 2100655 (2022).

[33] A. S. Doroshkevich, A. S. Zakharova, B. L. Oksengendler *et al.*, Nanomaterials **12**, 4493 (2022).

[34] M. N. Mirzayev, K. M. Hasanov, A. C. Parau *et al.*, J. Mater. Res. Technol. **27**, 1724 (2023).

[35] M. N. Mirzayev, A. C. Parau, L. Slavov *et al.*, Materials **16**, 1835 (2023).

[36] A. Vladescu, M. N. Mirzayev, A. S. Abiyev *et al.*, Nucl. Mater. Energy **35**, 101457 (2023).

[37] E. Popov, L. Slavov, E. Demir *et al.*, Vacuum **215**, 112338 (2023).

[38] A. V. Maletskyi, T. E. Konstantinova, G. K. Volkova *et al.*, Ceram. Int. **49**, 16044 (2023).

[39] L. Chkhartishvili, S. Makatsaria, N. Gogolidze *et al.*, Condens. Matter **8**, 92 (2023).

[40] S. F. Samadov, A. S. Abiyev, A. G. Asadov *et al.*, Ceram. Int. **50**, 3727 (2023).

[41] M. N. Mirzayev, A. S. Abiyev, O. A. Samedov *et al.*, J. Alloys Compd. **1005**, 175970 (2024).

[42] M. N. Mirzayev, G. T. Imanova, D. Neov *et al.*, J. Porous Mater. **31**, 1541 (2024).

[43] S. F. Samadov, A. S. Abiyev, A. G. Asadov *et al.*, Ceram. Int. **50**, 3727 (2024).

[44] S. F. Samadov, A. G. Asadov, A. S. Abiyev *et al.*, Physica B **688**, 416154 (2024).

[45] M. N. Mirzayev, E. D. Mustafayev, I. I. Mustafayev *et al.*, Radiat. Phys. Chem. **224**, 112008 (2024).

[46] S. F. Samadov, N. V. M. Trung, A. A. Donkov *et al.*, J. Nucl. Mater. **599**, 155242 (2024).

[47] E. P. Popov, A. A. Donkov, N. V. M. Trung *et al.*, Int. J. Refract. Met. Hard Mater. **124**, 106850 (2024).

[48] S. Makatsaria, L. Chkhartishvili, N. Barbakadze *et al.*, Solid State Sci. **154**, 107614 (2024).

[49] S. H. Jabarov, R. E. Huseynov, G. Sh. Ayyubova *et al.*, Solid State Commun. **386**, 115529 (2024).

[50] M. N. Mirzayev, S. H. Jabarov, E. B. Asgerov *et al.*, Results Phys. **10**, 541 (2018).

[51] M. N. Mirzayev, Kh. F. Mammadov, R. G. Garibov, E. B. Askerov, High Temp. **56**, 374 (2018).

[52] M. N. Mirzayev, R. N. Mehdiyeva, R. G. Garibov, N. A. Ismayilova, S. H. Jabarov, Mod. Phys. Lett. B **32**, 1850151 (2018).

[53] M. N. Mirzayev, R. N. Mehdiyeva, Kh. F. Mammadov, S. H. Jabarov, E. B. Asgerov, Phys. Part. Nucl. Lett. **15**, 673 (2018).

[54] M. N. Mirzayev, Kh. F. Mammadov, V. A. Skuratov *et al.*, J. Alloys Compd. **801**, 151 (2019).

[55] M. Mirzayev, E. Demir, Kh. Mammadov *et al.*, Int. J. Mod. Phys. B **33**, 1950073 (2019).

[56] M. N. Mirzayev, R. N. Mehdiyeva, S. Z. Melikova *et al.*, J. Korean Phys. Soc. **74**, 363 (2019).

[57] M. N. Mirzayev, Ceram. Int. **46**, 2816 (2020).

[58] M. N. Mirzayev, E. Demir, K. F. Mammadov *et al.*, J. Phys. **94**, 110 (2020).

[59] M. N. Mirzayev, Mod. Phys. Lett. B **34**, 2050395 (2020).

[60] M. N. Mirzayev, Int. J. Mod. Phys. B **34**, 2050160 (2020).

[61] M. N. Mirzayev, E. Popov, E. Demir *et al.*, J. Alloys Compd. **848**, 155119 (2020).

[62] M. N. Mirzayev, Vacuum **173**, 109162 (2020).

[63] M. N. Mirzayev, B. A. Abdurakhimov, S. H. Jabarov *et al.*, Int. J. Mod. Phys. B **34**, 2050008 (2020).

[64] M. N. Mirzayev, Radiat. Phys. Chem. **180**, 109244 (2021).

[65] M. N. Mirzayev, B. A. Abdurakhimov, E. Demir *et al.*, Physica B **611**, 412842 (2021).

[66] M. N. Mirzayev, L. Slavov, A. Donkov *et al.*, Radiat. Phys. Chem. **194**, 109988 (2022).

[67] E. Demir, E. Popov, M. Mirzayev *et al.*, Int. J. Refract. Met. Hard Mater. **106**, 105865 (2022).

[68] D. Neov, L. Slavov, A. A. Donkov *et al.*, Nucl. Mater. Energy **31**, 101201 (2022).

[69] D. R. Belichko, T. E. Konstantinova, G. K. Volkova *et al.*, Mater. Chem. Phys. **287**, 126237 (2022).

[70] E. Demir, M. N. Mirzayev, E. P. Popov *et al.*, Vacuum **184**, 109934 (2021).

[71] E. Demir, M. N. Mirzayev, A. B. Tugrul *et al.*, Surf. Rev. Lett. **27**, 1950169 (2020).

[72] E. Demir, M. N. Mirzayev, A. B. Tugrul *et al.*, Mod. Phys. Lett. B **33**, 1950216 (2019).